cence. At the CIS level, the energy needed to dissociate one NH_3 molecule from the cluster is calculated to be about the same as that available from the exoergicity of the H transfer reaction.

The configuration contributing dominantly to the excited wave function involves promotion of an electron from the highest occupied π orbital of 7HQ to the antibonding orbitals shown in Fig. 4 at different steps of the reaction. For the enol, this is the antibonding π^* orbital of 7HQ shown in Fig. 4A, whereas for HT1 it is an antibonding σ^* orbital on the newly generated NH_4 moiety (Fig. 4B). Accompanying this change of excited-state character is a transfer of about 0.9 electron from the 7HQ moiety to NH_3(1); i.e., the incipient proton transfer becomes a H atom transfer in the vicinity of $TS_{E/1}$. After passing the $TS_{E/1}$ barrier, the lowest excited state retains the $\pi\sigma^*$ character along the translocation coordinate up to $TS_{3/K}$. As seen in Fig. 4, B to D, the σ^* orbital accompanies the H atom as it moves along the ammonia wire via HT1, HT2, and HT3. A reverse σ^* $\rightarrow \pi^*$ state switching occurs near $TS_{3/K}$; the 7KQ orbital shown in Fig. 4E is a π^* orbital similar to that of the enol.

The $\pi^* \rightarrow \sigma^* \rightarrow \pi^*$ crossovers correlate with large changes of oscillator strength for the $S_1 \rightarrow S_0$ transition: In C_s symmetry, fluorescence is allowed from the $\pi\pi^*$ but forbidden from the $\pi\sigma^*$ state. Even without symmetry, this selection rule holds approximately: The calculated $S_1 \rightarrow S_0$ oscillator strength from the 7KQ $\pi\pi^*$ state is $f = 0.294$, whereas from the $\pi\sigma^*$-type states of HT1 to HT3 the f values vary from 0.001 to 0.004. This difference explains why the HT1, HT2, and HT3 forms have much longer radiative lifetimes and why no fluorescence is observed from these intermediates.

We show that single-file H atom transfer can be induced along the ammonia wire of the 7-hydroxyquinoline·$(NH_3)_3$ cluster. The reaction is initiated by $S_1 \leftarrow S_0$ excitation of 7-hydroxyquinoline but does not proceed from the vibrationless S_1 state. Additional excitation of S_1 state ammonia-wire solvent vibrations is necessary to activate the reaction. The measured reaction threshold is only 2.5 kJ mol^{-1}, increasing to 6 kJ mol^{-1} when fully deuterating the ammonia wire. Ab initio calculations of the S_1 and S_2 states predict a crossing of $\pi\pi^*$ and $\pi\sigma^*$ potential energy curves along the H atom transfer coordinate (21–25) that creates an initial barrier of ~44 kJ mol^{-1}. The first reaction step involves quantum tunneling from the ground state of the O–H mode. It is exothermic by about 30 kJ mol^{-1}, which provides the driving force for the subsequent reaction steps. The ammonia-wire modes that characterize the entrance channel region of the reaction are amenable to detailed spectroscopic investigations both below and above the reaction threshold and will allow state-specific kinetic investigations. The vibrational

energy and deuteration dependences underline the crucial role of the solvent coordinates on the tunneling rate (1, 9–13).

References and Notes
1. D. Borgis, J. Hynes, *Chem. Phys.* **170**, 315 (1993).
2. N. Agmon, *Chem. Phys. Lett.* **244**, 456 (1995).
3. D. Marx, M. E. Tuckerman, J. Hutter, M. Parrinello, *Nature* **397**, 601 (1999).
4. P. L. Geissler, C. Dellago, D. Chandler, J. Hutter, M. Parrinello, *Science* **291**, 2121 (2001).
5. D. Lu, G. A. Voth, *J. Am. Chem. Soc.* **120**, 4006 (1998).
6. R. Vuilleumier, D. Borgis, *J. Phys. Chem. B* **102**, 4261 (1998).
7. H. S. Mei, M. E. Tuckerman, D. E. Sagnella, M. L. Klein, *J. Phys. Chem. B* **102**, 10446 (1998).
8. R. Pomès, B. Roux, *Biophys. J.* **82**, 2304 (2002).
9. R. I. Cukier, D. G. Nocera, *Annu. Rev. Phys. Chem.* **49**, 337 (1998).
10. R. I. Cukier, J. Zhu, *J. Chem. Phys.* **110**, 9587 (1999).
11. P. K. Agarwal, S. P. Webb, S. Hammes-Schiffer, *J. Am. Chem. Soc.* **122**, 4803 (2000).
12. J. T. Hynes, T.-H. Tran-Thi, G. Granucci, *J. Photochem. Photobiol. A* **154**, 3 (2002).
13. Q. Cui, M. Karplus, *J. Phys. Chem. B* **106**, 7927 (2002).
14. Materials and methods are available as supporting material on *Science* Online.
15. S. F. Mason, J. Philip, B. E. Smith, *J. Chem. Soc. A* **1968** 3051 (1968).
16. S. Schulman, Q. Fernando, *Tetrahedron* **24**, 1777 (1968).
17. A. Bach, S. Leutwyler, *J. Chem. Phys.* **112**, 560 (2000).
18. M. Meuwly, A. Bach, S. Leutwyler, *J. Am. Chem. Soc.* **123**, 11446 (2001).
19. K. Tokumura, M. Itoh, *J. Phys. Chem.* **88**, 3921 (1984).
20. E. Bardez, *Isr. J. Chem.* **39**, 319 (1999).
21. A. L. Sobolewski, W. Domcke, *J. Phys. Chem. A* **103**, 4494 (1999).
22. A. L. Sobolewski, W. Domcke, *Phys. Chem. Chem. Phys.* **1**, 3065 (1999).
23. A. L. Sobolewski, W. Domcke, *J. Phys. Chem. A* **105**, 9275 (2001).
24. A. L. Sobolewski, W. Domcke, C. Dedonder-Lardeux, C. Jouvet, *Phys. Chem. Chem. Phys.* **4**, 1093 (2002).
25. O. David, C. Dedonder-Lardeux, C. Jouvet, *Int. Rev. Phys. Chem.* **21**, 499 (2002).
26. K. Daigoku, S. Ishiuchi, M. Sakai, M. Fujii, K. Hashimoto, *J. Chem. Phys.* **119**, 5149 (2003).
27. This work was supported by the Schweizerische Nationalfonds (project number 2000-68081.02) and by the Centro Svizzero di Calcolo Scientifico in Manno, Switzerland.

Direct Detection of the Yarkovsky Effect by Radar Ranging to Asteroid 6489 Golevka

Steven R. Chesley,[1]* Steven J. Ostro,[1] David Vokrouhlický,[2] David Čapek,[2] Jon D. Giorgini,[1] Michael C. Nolan,[3] Jean-Luc Margot,[4] Alice A. Hine,[3] Lance A. M. Benner,[1] Alan B. Chamberlin[1]

Radar ranging from Arecibo, Puerto Rico, to the 0.5-kilometer near-Earth asteroid 6489 Golevka unambiguously reveals a small nongravitational acceleration caused by the anisotropic thermal emission of absorbed sunlight. The magnitude of this perturbation, known as the Yarkovsky effect, is a function of the asteroid's mass and surface thermal characteristics. Direct detection of the Yarkovsky effect on asteroids will help constrain their physical properties, such as bulk density, and refine their orbital paths. Based on the strength of the detected perturbation, we estimate the bulk density of Golevka to be $2.7^{+0.4}_{-0.6}$ grams per cubic centimeter.

The Yarkovsky effect is a weak nongravitational acceleration believed to act on asteroids and meteoroids. According to theory (1–6), absorbed solar radiation is re-emitted in the infrared with some delay, which is related to the thermal inertia of the surface. This delay, in concert with the object's orbital and rotational motion, offsets the direction of the thermal

emission and its associated recoil force from the Sun's direction, resulting in a slow but steady drift in the semimajor axis of the object's orbit. Over millions of years, this drift can move main-belt asteroids and meteoroids until they reach a resonance, at which point gravitational perturbations take over and reroute them into the inner solar system (3, 7–9). The Yarkovsky effect also explains meteorite cosmic-ray exposure ages that are too long for the classical delivery scenarios (3, 10) and the large dispersion of asteroid family members that would otherwise have required unrealistically large collisional ejection velocities (6, 11). It can also limit the long-term predictability of possibly hazardous close-Earth approaches (12). The Yarkovsky effect has been detected in the motion
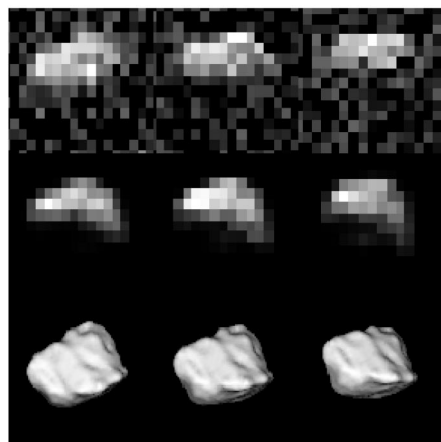
[1]Jet Propulsion Laboratory, California Institute of Technology, Pasadena, CA 91109, USA. [2]Institute of Astronomy, Charles University, CZ-18000 Prague 8, Czech Republic. [3]Arecibo Observatory, National Astronomy and Ionosphere Center, Arecibo, PR 00612, USA. [4]Department of Earth and Space Sciences, University of California, Los Angeles, CA 90095, USA.

*To whom correspondence should be addressed. E-mail: steven.chesley@jpl.nasa.gov

of artificial Earth satellites (*13*) but not for any natural bodies. Vokrouhlický *et al.* (*14*, *15*) explored the possibility of direct detection by means of the precise determination of near-Earth asteroid (NEA) orbits and concluded that such a detection would be feasible for NEAs up to a few kilometers in size, given precise radar astrometry spanning a decade or more. In particular, they predicted that radar ranging in May 2003 to the asteroid 6489 Golevka (which has a 530-m diameter) would reveal direct evidence for Yarkovsky accelerations. Here, we report the outcome of that radar experiment, which confirms Yarkovsky-induced modification of asteroid orbits.

Measurements of the distribution of radar echo power in time delay (range) and Doppler frequency (radial velocity) constitute two-dimensional images that can spatially resolve asteroids. The fine fractional precision of radar time-delay measurements and their orthogonality to optical plane-of-sky angular astrometry make them powerful for refining orbits (*16*). Radar observations of Golevka were conducted during its close-Earth approaches in 1991, 1995, and 1999. Delay-Doppler measurements were made at Arecibo, PR, and Goldstone, CA, in 1991 (*17*) and extensively at Goldstone in 1995 (*18*). The asteroid's shape and spin state were determined from the 1995 radar results (*18*). We imaged Golevka from Arecibo on 24, 26, and 27 May 2003 (Fig. 1), during the asteroid's closest Earth approach until 2046. With the shape model
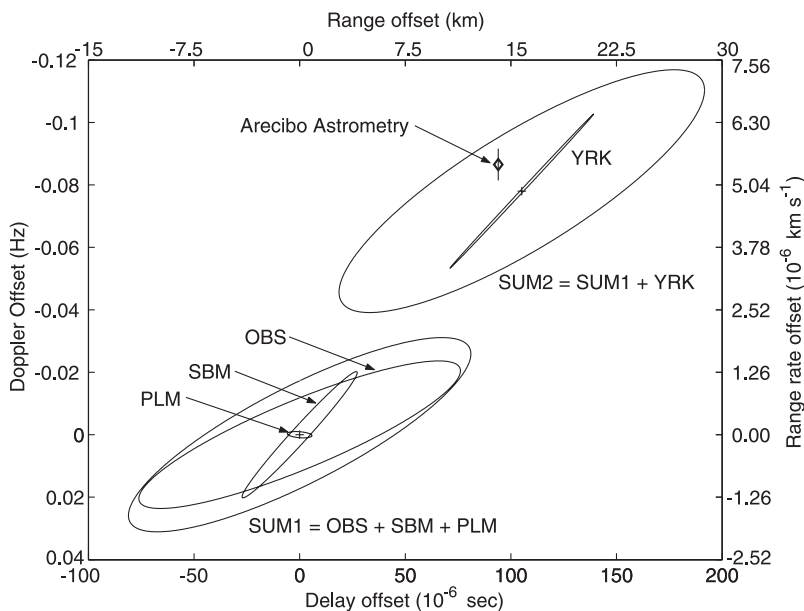
(*18*), we used least squares to estimate the location in each image of Golevka's center of mass (COM) (table S1). The radar time delays from 1991 were originally referenced to the peak power of the delay-Doppler distribution (*17*). Delay measurements from the 1995 observations (*18*) were referenced to the COM under the assumption that the COM was 390 m beyond the echo's leading edge in each image, whereas the shape model indicates that the range from the leading edge to the COM for those observations varied from about 225 m to about 320 m. Using images synthesized from the shape model, we reanalyzed the 1991 and 1995 images to estimate revised time delays, which are uniformly referenced to the COM (table S1).

We used a nonlinear numerical Yarkovsky model incorporating Golevka's radar-derived shape and spin state (*18*) to compute the Yarkovsky effect (*19*). The Yarkovsky acceleration depends on a number of physical parameters, including the spin state, which is known for Golevka, the surface conductivity K and the surface density ρ_s, which affect the strength of the recoil force, and the bulk density ρ_b, which only affects the acceleration through the asteroid's mass (*20*). Although our prediction is uncertain, we can place constraints on these parameters if the Yarkovsky effect can be measured. However, the principal measurable feature of the

Yarkovsky effect is a drift in the asteroid's mean anomaly that is quadratic with time and is caused by a linear semimajor axis drift da/dt (fig. S1). Because the perturbation is manifested only through the anomaly variation, the signatures of the individual parameters are not separable. The dependence on the bulk density is trivial ($da/dt \propto \rho_b^{-1}$), whereas the parameters K and ρ_s affect da/dt in a complicated way but only through their product $K\rho_s$ (*4*).

Asteroid surface thermal conductivities range from as low as 10^{-4} to 10^{-3} W m^{-1} K^{-1} for highly particulate surfaces [from both laboratory experiments (*21*) and observations (*22*, *23*)] to as high as 0.1 to 1 W m^{-1} K^{-1} for bare-rock surfaces of ordinary chondrite meteorites (*24*). The latter value drops by an order of magnitude when surface porosity increases from 0 to 10% (*24*). The steep surface gravitational slopes of Golevka (*18*) suggest a surface comprising both porous rock and thin regolith, which leads us to conclude that, for Golevka, K should be in the range 10^{-3} to 10^{-1} W m^{-1} K^{-1}. Golevka is classified as a Q-class asteroid (*25*). Whereas there are as of yet no measured Q-class densities, there are several known for the mineralogically related S-class asteroids (*19*). Consistent with these results, we have assumed an a priori bulk density of $\rho_b = 2.5$ g cm^{-3} and a surface density of $\rho_s = 1.7$ g cm^{-3}, because of presumed porosi-

Fig. 1. Arecibo delay–Doppler images of Golevka (top row) along with corresponding synthesized images based on the shape model (*18*) (middle row) and plane-of-sky views of that model (bottom row). The 24, 26, and 27 May results are shown in the left, middle, and right columns, respectively. Each of the nine frames is a 1.0-km square centered on Golevka's COM. In the radar images, time delay increases from top to bottom and Doppler frequency increases from left to right. The delay resolution is 0.5 μs (75 m in range) and the Doppler resolution is 0.238 Hz, or about 60 m, depending on the observing geometry. North is up in the plane-of-sky views. The images are sums of data from an average of six transmit-receive cycles and span an average of 18° of rotation phase.

Fig. 2. Predicted Yarkovsky-induced offset with 90% confidence ellipses in the space of radar delay (range) and Doppler (range rate) measurements on 26 May 2003 09:38 UTC. (The depiction is similar for the other radar observation dates in May 2003.) The predictions are based on astrometric data from April 1991 through October 1999, which marked the end of the previous apparition, and do not include observations made during the April to May 2003 observing apparition. The Yarkovsky prediction assumes the nominal values $\rho_b = 2.5$ g cm^{-3} and $K = 0.01$ W m^{-1} K^{-1}. Ellipses labeled OBS, SBM, PLM, and YRK represent the dispersions caused by uncertainties in astrometric measurements, small body masses, planetary masses, and Yarkovsky modeling, respectively. The SUM1 ellipse, which is the combination of the OBS, SBM, and PLM uncertainties, depicts the 90% confidence region for a non-Yarkovsky prediction. Similarly, the SUM2 ellipse, which includes the added uncertainty of the Yarkovsky modeling (*19*), represents the 90% confidence region for the prediction with Yarkovsky accelerations. The actual Arecibo radar delay and derived Doppler (*19*) measurement at this epoch is shown by a diamond with error bar.

ty and particulate matter on the asteroid surface.

The prediction of the orbit of Golevka is uncertain because of noise in the measured astrometric positions and uncertainties in the forces acting on the asteroid. The most significant force-modeling errors arise from solar radiation pressure, gravitational perturbations from the planets and other asteroids, and the Yarkovsky effect (12). For Golevka, we considered the prediction errors at the time of the 26 May 2003 radar observation,

12 years after discovery (Fig. 2). We found that direct and reflected radiation pressure causes a minor shift of only 2 to 3 μs in the predicted delay (19). Similarly, planetary masses are well determined and associated uncertainties can affect the prediction for Golevka by just 2 to 3 μs (19). The masses of perturbing asteroids, however, are very poorly constrained, and this represents a larger source of prediction uncertainty, ~13 μs at 1σ for Golevka (19). The modeled Yar-
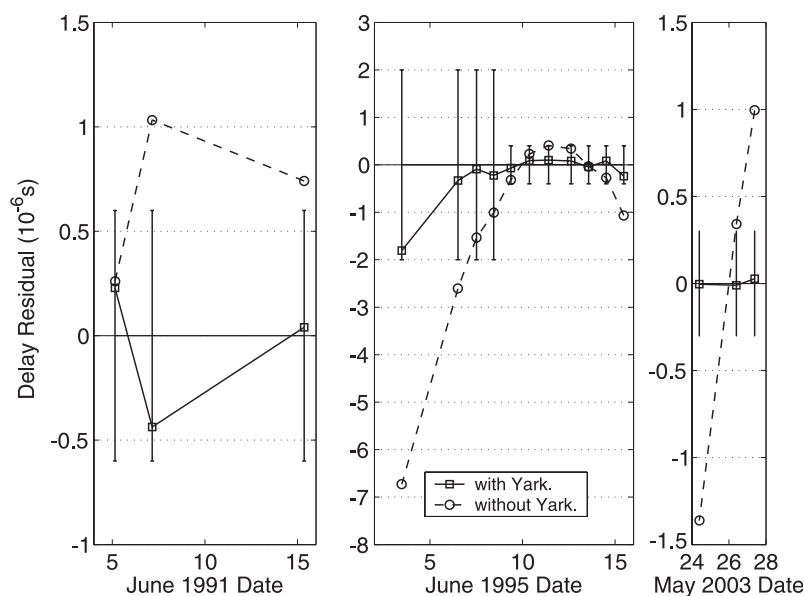
kovsky acceleration uncertainty is dominated by uncertainty in the bulk density and surface thermal conductivity of Golevka. Sensitivity tests indicated 1σ dispersions on the order of 16 μs because of realistic uncertainties on these parameters (19).

The separation between the Yarkovsky and non-Yarkovsky orbital predictions (Fig. 2) is about 15 km of range or 100 μs in radar delay, a 6σ discrepancy with respect to the non-Yarkovsky prediction. Thus, none of the estimated uncertainties are large enough to obscure the Yarkovsky effect. The actual Arecibo astrometry falls at 7.5σ from the non-Yarkovsky prediction and 1.3σ from the Yarkovsky prediction (Fig. 2). The formal probabilities of a measurement falling at or beyond these significance levels are $\sim 10^{-12}$ and 0.43, respectively.

An alternative approach to testing for Yarkovsky acceleration is to use all of the available optical and radar observations and consider how well they fit a particular force model. For Golevka, such fits are unacceptably poor when Yarkovsky accelerations are not used, whereas excellent fits are obtained with Yarkovsky accelerations (Fig. 3). In the latter case, one can fix the Yarkovsky acceleration by fixing ρ_b and K, or one can estimate one or the other of the two parameters. Varying either of these parameters only affects the mean anomaly of the orbit, so they are fully correlated and cannot be simultaneously estimated. Even so, we can form a constraint in (ρ_b, K)–space by estimating ρ_b for a variety of assumed values of K (Fig. 4), or vice versa. For bulk densities in the expected range (2.5 ± 0.5 g cm^{-3}) we find $K > 10^{-3}$ W m^{-1} K^{-1} (Fig. 4). Alternatively, if we assume that K falls in the interval from $10^{-2.5}$ to $10^{-1.5}$ W m^{-1} K^{-1}, then we infer a bulk density of 2.1 to 3.1 g cm^{-3}. Fixing $K = 10^{-2}$ W m^{-1} K^{-1} yields $\rho_b = 2.7 \pm 0.2$ g cm^{-3}, which we take to be the best fitting value and which implies a mass of 2.1×10^{11} kg (20). Based on the mean bulk density of ordinary chondrite meteorites, 3.34 g cm^{-3} (26), the macroporosity p of Golevka is 19% with a range of 7 to 37%, placing it within the "fractured" group of asteroids (27). These values of ρ_b and p are comparable to values estimated for much larger S-class asteroids (27).
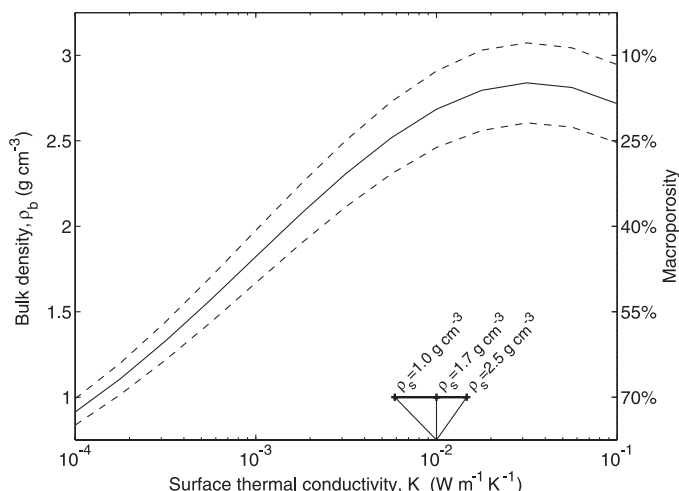
As radar tracking of NEAs continues, Golevka is likely to be only the first of many objects with detectable Yarkovsky accelerations (14). This suggests that the effect will eventually become a crucial component of precision orbit determination for small asteroids, in much the same way that nongravitational accelerations on comets are routinely computed.

The analyses described here can be used to estimate the physical properties of any small NEA for which a sufficient set of radar astrometry can be acquired. If additional observations that would allow decorrelation of ρ_b and K were available (such as infrared or radar backscatter observations) this technique

Fig. 3. Radar delay residuals for all Golevka range measurements (table S1). The residuals are the differences between the measured position and the computed postfit prediction. They are expected to be generally smaller than the measurement standard errors, which are indicated by error bars. Residuals that are systematically inconsistent with the measurement errors are indicative of mismodeling, in this case because of the absence of Yarkovsky accelerations in the asteroid force model. In addition to the depicted delay measurements, the fits included 748 right ascension/declination measurements from 15 April 1991 to 22 May 2003. Residuals from fits without the Yarkovsky effect are markedly worse than those from fits with the Yarkovsky effect. For solutions with and without the Yarkovsky acceleration, the root mean square values of the 20 delay residuals, normalized by the assigned measurement uncertainties, are 0.42 and 1.82, respectively.

Fig. 4. Estimated bulk density ρ_b of Golevka as a function of the assumed thermal conductivity K. Dashed curves indicate the extent of the formal error estimate. The ρ_b and K constraints assume a surface density of $\rho_s = 1.7$ g cm^{-3}; varying ρ_s over a reasonable range causes a shift in the abscissa as depicted at the bottom of the plot. The maximum in the curve is positioned fortuitously, allowing us to place an independent upper bound $\rho_b < 3.1$ g cm^{-3}. Values from the lower

left of the plot are inconsistent with probable values for both density and thermal conductivity; however, strictly independent lower limits cannot be determined. The descending branch of the curve for $K > 10^{-1}$ W m^{-1} K^{-1} (29) allows reasonable densities, but with unrealistically high conductivities. The macroporosity ordinate is based on the mean bulk density of type L ordinary chondrite meteorites, which is 3.34 g cm^{-3} (26).

would be strengthened. Still, apart from the roughly one-sixth of the NEA population thought to be binary systems (*28*), measuring the strength of the Yarkovsky acceleration offers the only means of estimating the masses of sub-kilometer NEAs from Earth-based observations.

References and Notes

1. D. P. Rubincam, *J. Geophys. Res.* **100**, 1585 (1995).
2. D. P. Rubincam, *J. Geophys. Res.* **103**, 1725 (1998).
3. P. Farinella, D. Vokrouhlický, W. K. Hartmann, *Icarus* **132**, 378 (1998).
4. D. Vokrouhlický, *Astron. Astrophys.* **335**, 1093 (1998).
5. D. Vokrouhlický, *Astron. Astrophys.* **344**, 362 (1999).
6. W. F. Bottke, D. Vokrouhlický, D. P. Rubincam, M. Brož, in *Asteroids III*, W. F. Bottke Jr., A. Cellino, P. Paolicchi, R. P. Binzel, Eds. (Univ. Arizona Press, Tucson, AZ, 2003), pp. 395–408.
7. W. F. Bottke, D. P. Rubincam, J. A. Burns, *Icarus* **145**, 301 (2000).
8. P. Farinella, D. Vokrouhlický, *Science* **283**, 1507 (1999).
9. A. Morbidelli, D. Vokrouhlický, *Icarus* **163**, 120 (2003).
10. D. Vokrouhlický, P. Farinella, *Nature* **407**, 606 (2000).
11. W. F. Bottke, D. Vokrouhlický, M. Brož, D. Nesvorný, A. Morbidelli, *Science* **294**, 1693 (2001).
12. J. D. Giorgini *et al.*, *Science* **296**, 132 (2002).
13. D. P. Rubincam, *J. Geophys. Res.* **92**, 1287 (1987).
14. D. Vokrouhlický, A. Milani, S. R. Chesley, *Icarus* **148**, 118 (2000).
15. D. Vokrouhlický, S. R. Chesley, A. Milani, *Celest. Mech. Dyn. Astron.* **81**, 149 (2001).
16. D. K. Yeomans, S. J. Ostro, P. W. Chodas, *Astron. J.* **94**, 189 (1987).
17. S. J. Ostro *et al.*, *Bull. Am. Astron. Soc.* **23**, 1144 (1991).
18. R. S. Hudson *et al.*, *Icarus* **148**, 37 (2000).
19. Materials and methods are available as supporting material on *Science* Online.
20. The asteroid's mass and bulk density are related through the volume of the shape model, which is 7.79465×10^7 m³ (*18*).
21. A. E. Wechsler, P. E. Glaser, A. D. Little, J. A. Fountain, in *Thermal Characteristics of the Moon*, J. W. Lucas, Ed. (MIT Press, Cambridge, MA, 1972), pp. 215–242.
22. A. W. Harris, J. S. V. Lagerros, in *Asteroids III*, W. F. Bottke Jr., A. Cellino, P. Paolicchi, R. P. Binzel, Eds. (Univ. Arizona Press, Tucson, AZ, 2003), pp. 205–218.
23. M. G. Langseth, E. M. Drake, D. Nathanson, J. A. Fountain, in *Thermal Characteristics of the Moon*, J. W. Lucas, Ed. (MIT Press, Cambridge, MA, 1972), pp. 169–204.
24. K. Yomogida, T. Matsui, *J. Geophys. Res.* **88**, 9513 (1983).
25. S. J. Bus, R. P. Binzel, *Icarus* **158**, 146 (2002).
26. G. J. Consolmagno, D. T. Britt, C. P. Stoll, *Meteorit. Planet. Sci.* **33**, 1221 (1998).
27. D. T. Britt, D. Yeomans, K. Housen, G. Consolmagno, in *Asteroids III*, W. F. Bottke Jr., A. Cellino, P. Paolicchi, R. P. Binzel, Eds. (Univ. Arizona Press, Tucson, AZ, 2003), pp. 485–500.
28. J. L. Margot *et al.*, *Science* **296**, 1445 (2002).
29. S. R. Chesley *et al.*, data not shown.
30. We thank V. Negrón and the technical staff of the Arecibo Observatory for help with the radar observations; G. Garrad, W. Owen Jr., and T. Spahr for providing precise optical astrometry of Golevka; and S. Hudson for providing his shape reconstruction software. This research was conducted in part at the Jet Propulsion Laboratory, California Institute of Technology under a contract with NASA. Additional support was provided by the Grant Agency of the Czech Republic. The Arecibo Observatory is part of the National Astronomy and Ionosphere Center, which is operated by Cornell University under a cooperative agreement with NSF and with support from NASA.

Supporting Online Material
www.sciencemag.org/cgi/content/full/302/5651/1739/DC1
Materials and Methods
Fig. S1
Table S1
References

12 September 2003; accepted 30 October 2003

Water Isotope Ratios D/H, ^{18}O/^{16}O, ^{17}O/^{16}O in and out of Clouds Map Dehydration Pathways

Christopher R. Webster[1]* and Andrew J. Heymsfield[2]

Water isotope ratios have been measured by laser absorption spectroscopy in and out of cirrus clouds formed in situ and convectively generated in anvils over subtropical regions. Water vapor in the tropical and subtropical upper troposphere shows a wide range of isotopic depletion not observed previously. The range suggests that dehydration of upper tropospheric air occurs both by convective dehydration and by gradual dehydration mechanisms. Twenty-five percent of upper tropospheric water sampled is in ice particles whose isotopic signatures are used to identify those grown in situ from those lofted from below.

Tropospheric water vapor is the most important greenhouse gas and a key component of the climate system (*1*). In the upper troposphere (UT) and lower stratosphere (LS), water vapor, liquid clouds, and ice particles substantially affect the radiation balance, atmospheric circulation, and chemistry (*2*). Cirrus clouds in particular affect UT water ice and vapor content, which global climate models indicate have large effects on Earth's radiative balance (*3–5*), especially in the dry subtropical UT (*6*).

Understanding the sources and sinks of water in the UT and LS and the mechanism of stratospheric dehydration is one of the important remaining challenges in Earth science, because water vapor feedback mechanisms can increase ozone depletion (*7*) and lead to stratospheric cooling (*8*). A doubling in stratospheric humidity over the last half century has been reported (*9*), despite decreasing tropical tropopause temperatures (*10*).

The extent to which the humidity of air transported from the troposphere into the stratosphere is controlled by tropopause minimum temperatures, cloud microphysics and convection, and mixing of air between high and low latitudes is not fully understood. The water vapor content of air entering the LS [3 to 4.1 parts per million volume (ppmv) (*11*)] is lower than the ice saturation mixing ratio (~4.5 ppmv) that would be determined by freeze-drying at the global mean tropopause temperature. Although there is consensus that dehydration occurs principally in the tropical tropopause layer (TTL) [covering the altitude range from ~13 to 19 km (*12, 13*)], two competing mechanisms have been proposed: "convective dehydration" and "gradual dehy-

dration" (*13*). Convective dehydration results from rising air masses overshooting their level of neutral buoyancy (LNB) to become severely dehydrated ($\leq$1 ppmv by condensation and fallout) before mixing (*14–18*) with moister air. In gradual dehydration (*13, 19–21*), air detrains from convection near its LNB at the bottom of the TTL and becomes dehydrated during slow ascent through regions that have temperatures below the tropopause global average temperature. This "cold trap" region need not be the local tropopause for a sampled air parcel, because time scales for horizontal versus vertical transport allow air parcels to "visit" far away cold pools such as that of the tropical Western Pacific (*13*).

Water vapor has a long lifetime (*22*), has an observed seasonal cycle (*19, 23*), and is a good tracer of atmospheric transport. Its stable isotopes, especially HDO and $H_2^{18}O$ compared with $H_2^{16}O$, suffer large fractionations in an air parcel [expressed as delta-D (δD) and delta-^{18}O (δ^{18}O) (*24*), respectively] as a result of condensation and sedimentation (*25*). Since the first tropospheric (*26*) and stratospheric (*27*) HDO measurements, subsequent studies (*28–33*) have recognized that water isotope fractionation is, in principle, a sensitive tracer for diagnosing transport and dehydration mechanisms.

Gradual dehydration is expected to follow Rayleigh distillation (*34*) in which all condensate is removed during adiabatic cooling. In this case, the vertical profile of δD for atmospheric water vapor is expected to begin at ~−86 per mil (‰) above the ocean [standard mean ocean water (SMOW) is 0‰ (*35*)] and reduce monotonically to ~−950‰ at the coldest tropopause. Few in situ measurements exist, particularly in tropical regions. Before the work presented here, such low values were usually not observed [except −837 ± 100‰ (*36*) in the polar vortex, and −810 ± 213‰ in the UT over Texas (*37*)]. At mid- and low-latitudes, UT values down to −670‰ have been reported (*38*).

[1]Earth and Space Sciences Division, Jet Propulsion Laboratory (JPL), California Institute of Technology, Pasadena, CA 91109, USA. [2]National Center for Atmospheric Research (NCAR), Boulder, CO 80301, USA.

*To whom correspondence should be addressed. E-mail: chris.r.webster@jpl.nasa.gov